

Imaging a Chain of Rydberg Superatoms Enabled by Förster-Resonance-Enhanced Interaction

Jinjin Du^{1,*}, Thibault Vogt^{2,1,*†}, Ningxuan Zheng¹, and Wenhui Li^{1,3††}

Centre for Quantum Technologies, National University of Singapore, 3 Science Drive 2, Singapore 117543¹

School of Physics and Astronomy, Sun Yat-sen University, Zhuhai, 519082, China² and

State Key Laboratory of Quantum Optics and Quantum Optics Devices and
Institute of Opto-Electronics, Shanxi University, Taiyuan 030006, China³

We demonstrate single-shot and *in situ* absorption imaging of individual Rydberg superatoms. This level of resolution is achieved using an electromagnetically induced transparency scheme involving a Rydberg energy level that is highly sensitive to the presence of Rydberg superatoms due to Förster-resonance-enhanced dipole couplings. Spectroscopic measurements illustrate the existence of the Förster resonance and underscore the state-selectivity of the technique. With an imaging exposure time as short as $3\ \mu\text{s}$, we successfully resolve linear chains of Rydberg superatoms excited in a one-dimensional configuration. The extracted second-order correlation shows strong anti-bunching due to excitation blockade, and a Fourier analysis reveals the long-range order in the chains of Rydberg superatoms. This imaging technique, with minimal destruction, will be of great interest for leveraging ensemble-encoded qubits in quantum computation and quantum simulation applications.

PACS numbers: 42.50.Gy, 42.65.Ky, 32.80.Ee

I. INTRODUCTION

Highly excited Rydberg atoms have emerged as a prominent physical platform for applications in quantum nonlinear optics [1] and quantum simulation and computation [2, 3]. The essential element enabling the high degree of control and manipulation at the single-particle level in these systems is the strong long-range interaction between Rydberg atoms [4]. The resulting excitation blockade effect [5–8] leads to collective and entangled quantum states, which are important resources for quantum applications. Fascinating demonstrations in quantum optics include generating single-photon sources [9, 10], single-photon switches [11], phase gates [12], and contactless non-linear optics [13]. More recently, Rydberg-atom arrays, exploring the long-range interaction in ordered configurations, have made remarkable progress in simulating quantum many-body physics and advancing large-scale neutral-atom quantum computation [3, 14–17].

So far, the detection of Rydberg atoms has mostly relied on destructive means. For an extended period of time, state-selective field ionization served as the primary method for conducting measurements on Rydberg atoms [4]. It has recently been further developed into high-resolution ion microscopy [18–20]. When Rydberg excitations are induced in optical lattices or tweezer arrays, they are often detected via fluorescence imaging of ground-state atoms, where the loss of an atom at a particular tweezer or lattice location indicates its excitation to Rydberg states before measurement [21, 22].

The seminal work on electromagnetically induced transparency involving Rydberg states (Rydberg EIT) [23] has laid the foundation and paved the way for the direct optical detection of Rydberg excitations. In Rydberg EIT, long-range interactions can be mapped onto polaritons and detected by retrieving and counting the photons released from the polaritons [9, 10, 12, 13]. In the dissipative regime, capitalizing on the interaction-induced scattering effect, Rydberg EIT has recently been employed for nondestructive optical imaging of Rydberg excitations [24–26]. The long-range interaction between one Rydberg excitation and surrounding polaritons is responsible for a sharp change of transmission of EIT, which allows fast *in situ* imaging of the Rydberg excitation in a nondestructive way. This method has been used for imaging transport dynamics of Rydberg excitations, but without reaching single-particle resolution [24]. The latest development and applications of this detection approach include repeated nondestructive measurements of an ensemble-based Rydberg qubit [25], switching an atomically thin mirror by a single Rydberg atom [26], as well as fast imaging of individual ions in an atomic ensemble [27]. These experiments have proven that this ensemble-assisted method would be particularly suitable for detecting a Rydberg excitation within a mesoscopic ensemble or a Rydberg “superatom”, and is faster and less destructive compared to other means of detecting Rydberg atoms.

In this letter, we demonstrate spatially resolved imaging of a chain of Rydberg superatoms in a single shot with a $3\ \mu\text{s}$ exposure time. We reach this sensitivity by exploring a novel Förster-resonance scheme between a $27F$ state and a $96S$ state. The former serves as the upper level of the Rydberg EIT for detection, while the latter is the excitation state of the Rydberg superatoms under investigation. The enabling strong long-range interaction arises from a Förster-like resonance between the two

* These two authors contributed equally.

*† ttvogt@mail.sysu.edu.cn

†† liwenhui@sxu.edu.cn

pair states $|27F96S\rangle$ and $|27G95P\rangle$, which are strongly dipole-coupled. A distinctive feature here is the small principal quantum number, $n = 27$, which is far away from $n' = 96$, unlike previously used detection schemes where $n \sim n'$ [24–26]. Consequently, relatively large EIT probe power can be used without causing too much spurious scattering of $27F$ polaritons interacting with each other, and the read noise of the camera is easily overcome when homodyne detection is being employed. Spectroscopic measurements illustrate the working principle of the scheme and provide suitable conditions for single-shot imaging. From single-shot images of Rydberg superatoms aligned in a one-dimensional chain, the pair correlation function is extracted to reveal the excitation blockade. Moreover, spatial Fourier analysis shows the presence of long-range order in the chains of excited superatoms. This work marks a major advancement in achieving spatially-resolved, nondestructive detection of Rydberg superatoms. It holds particular significance in utilizing ensemble-assisted Rydberg qubits for quantum simulation and computation.

The paper is organized as follows. In Section II, we discuss the Förster resonance and experimentally demonstrate it with Rydberg EIT spectra, measuring the transmission of the EIT probe light at different probe frequency detunings. In Section III, we present single-shot images of individual Rydberg superatoms and, based on these images, analyze the excitation of these superatoms into a one-dimensional chain. It is important to note that, unlike the spectroscopic measurements in Section II, where only the EIT probe light is sent through the atomic cloud and projected onto the camera, the single-shot imaging in Section III is performed with the help of the homodyne detection technique [27]. We summarize our results and provide some outlook in Section IV. Additional experimental and calculation details are included in Appendices.

II. FÖRSTER-RESONANCE-ENHANCED INTERACTION

The basic principle of the imaging method relies on interaction induced absorption in the vicinity of Rydberg superatoms. In contrast to previously reported schemes, our approach explores an uncharted molecular resonance corresponding to the dipole-dipole-mediated energy exchange,

$$nF + n'S \Leftrightarrow nG + (n' - 1)P. \quad (1)$$

Here, nF is the upper state of Rydberg EIT, $n'S$ is the state of the Rydberg superatoms being detected, and n and n' are vastly different. As illustrated by the calculation in Fig. 1(a), for each principal quantum number around $n \sim 30$, there exists a specific $n' \sim 100$ such that the pair-state energy difference $|\Delta E| = |(E_{nF} + E_{n'S}) - (E_{nG} + E_{(n'-1)P})|$ is minimal. This minimal energy difference can be as small as

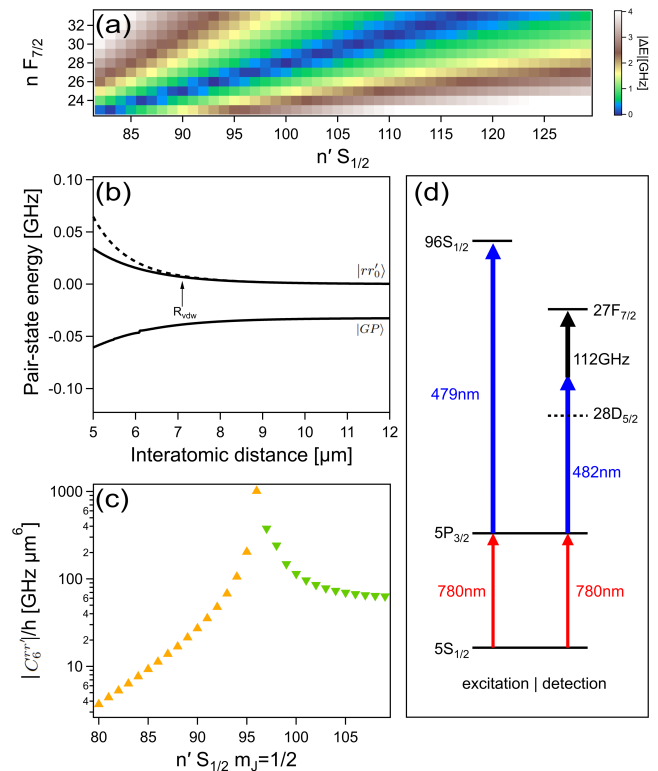


FIG. 1. (a) Pair-state energy difference $|\Delta E|$ (absolute value) for a range of n and n' at zero magnetic field $B = 0$. (b) Interaction potential curves of the two pair-states that asymptotically approach $|rr'_0\rangle = |27F_{7/2}, m_J = 7/2, 96S_{1/2}, m_J = 1/2\rangle$ and $|GP\rangle = |27G_{9/2}, m_J = 9/2, 95P_{3/2}, m_J = 3/2\rangle$ as $R \rightarrow \infty$ and in presence of a magnetic field $B = 13.3$ G. The latter pair-state is the one that most strongly couples to the former. The dashed line represents the van der Waals potential $V^{rr'_0}(R) = -C_6^{rr'_0}/R^6$ obtained from fitting the upper thick solid curve for $R > 1.3 \times R_{\text{vdW}} = 9.2 \mu\text{m}$ [28]. (c) Amplitude of the $C_6^{rr'}$ coefficients for a range of n' . Yellow (green) upwards (downwards) triangles correspond to negative (positive) values, indicating a repulsive (attractive) interaction. (d) Energy level schemes for Rydberg excitation and multi-photon EIT detection.

a few tens of MHz. For instance, at $n = 27$, the minimal $|\Delta E| = |(E_{27F_{7/2}} + E_{96S_{1/2}}) - (E_{27G_{9/2}} + E_{95P_{3/2}})|$ is approximately 80 MHz and can be even smaller than 50 MHz for certain pair states of Zeeman sublevels in the presence of a magnetic field. The large dipole-dipole coupling described in Eq. (1) can exceed the energy difference at a macroscopic distance R_{vdW} of a few microns, where the threshold dipole coupling is defined as $|\mu_{nFnG}\mu_{n'S(n'-1)P}|/R_{\text{vdW}}^3 = |\Delta E|/2$ with μ_{nFnG} and $\mu_{n'S(n'-1)P}$ being the two dipole moments between the pair-states from the left and the right of Eq. (1) respectively. Consequently, the pair interaction shift of the $|nFn'S\rangle$ state on the left side of Eq. (1) is Förster-resonance enhanced. That is, the van der Waals inter-

action $V(R) = -C_6/R^6$ between two atoms in these states, which is generally used to approximate the potential curve from $R = R_{vdW}$ until $R \rightarrow \infty$, can possess quite a sizable C_6 coefficient, despite the substantial difference between n' and n .

In our experiment, with the presence of a bias magnetic field of 13.3 G along the quantization axis \hat{z} , the $|r\rangle = |27F_{7/2}, m_J = 7/2\rangle$ state is used as the upper Rydberg EIT level to image Rydberg excitations in a Zeeman level $|r'_0\rangle = |96S_{1/2}, m_J = 1/2\rangle$. Shown in Fig. 1(b) are the interaction potential curves of the pair states $|rr'_0\rangle$ and $|GP\rangle = |27G_{9/2}, m_J = 9/2, 95P_{3/2}, m_J = 3/2\rangle$, which is the pair state most strongly dipole-coupled to $|rr'_0\rangle$. The small $\Delta E = 33$ MHz and strong dipole coupling ensure that the interaction potential of the pair state $|rr'_0\rangle$, $V^{rr'_0}(R) = -C_6^{rr'_0}/R^6$, possesses a large coefficient $C_6^{rr'_0}/h = -1010$ GHz $\cdot\mu\text{m}^6$. Here $C_6^{rr'_0}$ is extracted by fitting $V^{rr'_0}(R)$ to the potential curve for $R > 1.3 \times R_{vdW} = 9.2 \mu\text{m}$, which asymptotically converges to the $|rr'_0\rangle$ pair state as $R \rightarrow \infty$. Plotted in Fig. 1(c) is the interaction coefficient $C_6^{rr'}$, where $|r'\rangle = |n'S_{1/2}, m_J = 1/2\rangle$, for a range of n' . A resonant peak at $n' = 96$ can be clearly seen. In case a different detection state $n \neq 27$ is used, the resonance peak appears at a different excitation state n' , as implied by the plot of energy differences in Fig. 1(a). This indicates that this Förster-resonance enhanced interaction can allow state-selective imaging.

One advantage of this new scheme, utilizing an EIT detection state of low n for imaging a Rydberg excitation of a high n' state, is that the small interaction $V^{rr} = -C_6^{rr}/R^6$ between two atoms in the $|r\rangle$ state greatly reduces the photon scattering of the probe light [29, 30]. As a result, this scheme allows good EIT transmission at a large enough detection probe Rabi frequency Ω_p , which provides sufficient photon flux to surpass imaging noises under the condition of homodyne detection. Meanwhile, the interaction $V^{rr'_0}(R) = -C_6^{rr'_0}/R^6$ is quite large due to the existence of the Förster resonance shown in Eq. (1), even if the difference between n' and n is much larger than that typically used. These are the root causes of the increased sensitivity that warrants fast imaging of single Rydberg excitation.

A. Spectroscopic Measurements

We demonstrate the presence of the Förster-like resonance shown in Fig. 1(c) by spectroscopic measurements. We employ EIT involving the $|r\rangle$ upper state to detect Rydberg excitations in $|r'\rangle$ states, and the relevant energy levels are illustrated in Fig. 1(d). The interstate blockade radius is defined as $R_{b-r'} = [2|C_6^{rr'}|/(\hbar\gamma_{EIT})]^{1/6}$, where γ_{EIT} is the EIT linewidth. Inside the blockade sphere of radius $R_{b-r'}$ centered at each $|r'\rangle$ excitation, the shift of the $|r\rangle$ state due to $V^{rr'}(R)$ exceeds half of the imaging EIT linewidth γ_{EIT} and the atoms within

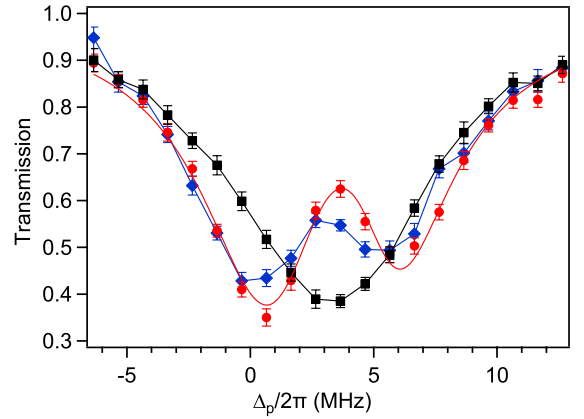


FIG. 2. Probe light EIT spectra without prior excitation of Rydberg superatoms (red circles) and with prior excitation of Rydberg superatoms in states $|r'_0\rangle$ (black squares) and $|r'_1\rangle$ (blue diamonds). $\Delta_P = 0$ corresponds to the resonance of the atomic transition $|g\rangle \rightarrow |e\rangle$ in the bias magnetic field $B = 13.3$ G. Due to the AC Stark shift caused by the off-resonance two-photon transition $|e\rangle \rightarrow |r\rangle$, the EIT peak appears around $\Delta_P/2\pi \simeq 3.65$ MHz. The error bars indicate the standard error of 15 measurements. The solid red line is a three-level EIT fit, and the other two solid lines provide a guide to the eye.

the sphere scatter the probe light. A larger $C_6^{rr'}$ leads to a larger $R_{b-r'}$ and consequently more absorption within the blockade sphere. Spectroscopic measurements discussed in this section show that the $|r'_0\rangle$ excitations induce more absorption than excitations in other states due to $C_6^{rr'_0}$ and the corresponding $R_{b-r'_0}$ being the largest.

The spectroscopic measurements are conducted in an elongated and dense atomic cloud of radius $\sigma_r = 6 \mu\text{m}$ and the $|r\rangle$ EIT spectra vs the frequency of the 780-nm probe light, as shown in Fig. 2, are recorded with or without prior Rydberg excitation. The experimental configuration is illustrated in Fig. 6 and detailed in Appendix B. The EIT spectrum with no Rydberg excitations present shows a pronounced EIT peak with up to about 50% transmission. The less than 100% transmission comes from the scattering due to the interaction $V^{rr}(R)$ between Rydberg atoms in the $|r\rangle$ state.

For acquiring EIT spectra in the presence of Rydberg impurities (Rydberg excitations amidst an atomic ensemble), we excite a one-dimensional chain of closely-packed Rydberg superatoms in the $|r'\rangle$ states along the elongated cloud, where the length of the atomic cloud exposed to the excitation lasers is $a_x = 350 \mu\text{m}$. By tuning the Rabi frequency of the 479-nm excitation field, we keep the excitation blockade radius to be $R_{b-EX}^{r'} = 14.5 \pm 0.2 \mu\text{m}$, which exceeds the radial size of the elongated atomic cloud $2\sigma_r$ (refer to Appendix B). Under such a condition, the excitation of Rydberg superatoms tends to be a one-dimensional (1D) chain and closely-packed, as demonstrated and explained further in the paper. Af-

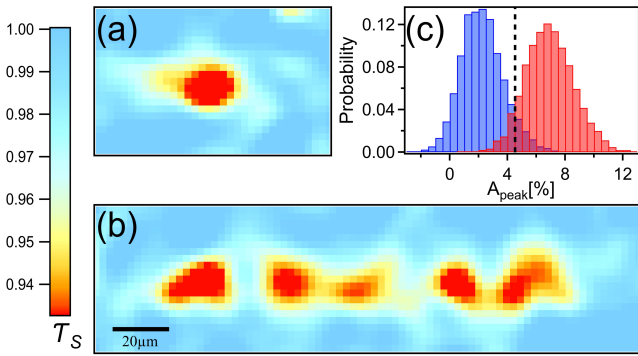


FIG. 3. (a) Gaussian smoothed (filter size = 2 pixels) single-shot image of one Rydberg superatom. (b) Gaussian smoothed (filter size = 2 pixels) single-shot image of a chain of 5 Rydberg superatoms. (c) Histogram of the peak amplitudes of the absorption spots inside the excitation area (red) vs. that in an area of the same size and shape along the atomic cloud (blue). The vertical dashed line indicates the threshold $A_{\text{thld}} = 4.5\%$. The statistical distributions are based on approximately 1200 single-shot images.

ter the excitation, the detection EIT fields are turned on for spectroscopy. When the excitation state is $|r'_1 = 85S_{1/2}, m_J = 1/2\rangle$, the resulting spectrum still shows a pronounced EIT peak that is slightly reduced from that with no Rydberg excitations present. However, when the excitation state is $|r'_0 = 96S_{1/2}, m_J = 1/2\rangle$, the transmission peak in this case completely disappears. This is despite the fact that the numbers of Rydberg superatoms excited per unit length are about the same for exciting the $|r'_1\rangle$ and $|r'_0\rangle$ states as the same $R_{b-EX}^{r'_i}$ is used. The spectroscopic responses are very different because $V^{rr'_0}(R)$ is much stronger than $V^{rr'_1}(R)$ given $C_6^{rr'_i}/h = -9.3 \text{ GHz}\cdot\mu\text{m}^6$. As a result, the interstate Rydberg-blockade sphere surrounding each Rydberg excitation has a radius of $R_{b-r'_1} = 4.0 \mu\text{m}$ vs. $R_{b-r'_0} = 8.7 \mu\text{m}$. There are only about 80 scattering atoms inside the blockade sphere of radius $R_{b-r'_1}$ surrounding a $|r'_1\rangle$ excitation, in comparison to approximately 600 inside that of radius $R_{b-r'_0}$ surrounding a $|r'_0\rangle$ excitation. Hence, the probe transmission is much reduced in the presence of a $|r'_0\rangle$ excitation. The resulting contrast between these spectra clearly shows the effect of the Förster resonance and illustrates the principle of this Förster-resonance-enhanced imaging scheme.

III. SINGLE-SHOT IMAGING OF A CHAIN OF RYDBERG SUPERATOMS

To clearly demonstrate single-shot imaging of individual Rydberg superatoms excited to the $96S$ state, we reduce the length of the atomic cloud exposed to the excitation lasers along the symmetry axis of the atomic cloud to $a_x = 126 \mu\text{m}$ or $a_x = 17 \mu\text{m}$. This is to re-

duce inhomogenous factors (e.g. atomic density along the elongated cloud), as well as to allow for a direct comparison of the cloud sections with and without excitations in single-shot images. In each experimental cycle, after exciting Rydberg superatoms, we capture an image of these atoms by exposing them to probe light under EIT conditions for $3 \mu\text{s}$, where the frequency of the probe is set to the EIT resonance position of $\Delta_P/2\pi = 3.65 \text{ MHz}$. Furthermore, we employ homodyne detection to achieve a sufficient signal-to-noise ratio for single-shot detection. This technique involves overlapping a strong reference beam with the probe light and detecting their interference with the camera (Appendix B). Further details of imaging with homodyne detection were given in our previous publication [27].

The way of processing these single-shot images of Rydberg superatoms is quite similar to that used in our previous work [27]. After fringe removal and normalization, the obtained transmission distribution $\mathcal{T}(x, y)$ over each pixel position (x, y) serves as the starting point for further quantitative analysis. Shown in Fig. 3 are smoothed images $\mathcal{T}_S(x, y)$ after applying Gaussian filtering to $\mathcal{T}(x, y)$. Pronounced absorption spots of one and five Rydberg “superatoms” are clearly visible in Figs. 3(a) and 3(b), respectively, where the excitation length a_x is set to be $a_x = 17 \mu\text{m}$ in the former case and $a_x = 126 \mu\text{m}$ in the latter case. From a single-shot image as in Fig. 3(b), we extract the peak amplitudes of absorption spots, defined as $A_{\text{peak}} = 1 - \mathcal{T}_{S\text{min}}$, where $\mathcal{T}_{S\text{min}}$ denotes local transmission minima, inside the area with Rydberg excitations. A histogram of such peak amplitudes out of many single-shot images are plotted in Fig. 3(c). To make comparison, we also plot the histogram of peak amplitudes of noise spots from another area along the atomic cloud that has the same size and shape, but no Rydberg excitation. The two distributions are well separated, and can be best distinguished by the threshold peak amplitude $A_{\text{thld}} = 4.5\%$. We evaluate the probability of identifying a Rydberg superatom in a single-shot image based on the distributions of Fig. 3(c), where the true negative probability (no Rydberg atom is detected when none is present) below A_{thld} is equal to the true positive probability (the presence of a Rydberg superatom is detected) above A_{thld} [31]. The fidelity of detecting a Rydberg atom is then defined as the true positive probability and estimated to be $(93 \pm 2)\%$.

Finally, this single-shot imaging allows us to investigate the ordered excitation of a linear Rydberg superatom array in a dense atomic cloud. The excitation blockade radius $R_{b-EX}^{r'_0} = 14.7 \mu\text{m}$ leads to a chain of Rydberg superatoms, corresponding to spheres of radius $R_{b-EX}^{r'_0}$ containing no more than one Rydberg atom, excited in a closely packed arrangement [32, 33]. Each imaging detection projects a Rydberg superatom into an absorption spot located within the blockade sphere of radius $R_{b-EX}^{r'_0}$. In Fig. 4(a), we plot the 2D distribution of the positions of Rydberg superatoms. Here the position

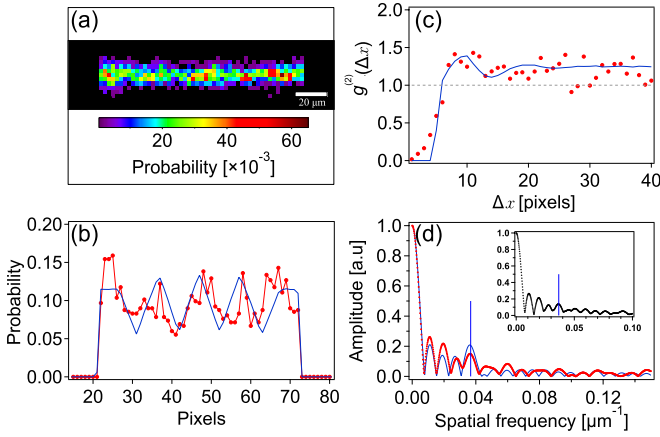


FIG. 4. (a) Two-dimensional (2D) distribution of the peak positions of 5 Rydberg superatoms. This figure is obtained from single-shot images with 5 absorption spots of $A_{peak} > A_{thld}$. (b) One-dimensional distribution along the x direction. The experimental data points (red markers) are derived by integrating along y the 2D distribution in (a), while the blue line is obtained from the simulation of a linear chain of five Rydberg superatoms. (c) Pair correlation function of the positions of Rydberg excitations in experimental single-shot images (red markers) and from simulated chains (blue line). (d) FFT spectrum of 1D spatial distributions in (b), extracted from experimental data (red markers) and from simulated distribution (blue line). The inset shows FFT spectrum of Rydberg superatom 1D distributions extracted from experimental images with 4 and 6 absorption spots of $A_{peak} > A_{thld}$. The solid vertical line is the same as that in (d).

of a Rydberg superatom is taken as the location of an absorption maximum with its amplitude above the threshold $A_{peak} > A_{thld}$. Five separated distribution peaks are visible in Fig. 4(a) as well as in Fig. 4(b).

To further study the 1D spatial correlation of the Rydberg “superatoms” chain along the x direction, we compute the 1D pair correlation function as a function of Δx

$$g^{(2)}(\Delta x) = \frac{5 \sum_i \langle n_{\text{ryd}}(x_i) \cdot n_{\text{ryd}}(x_i + \Delta x) \rangle}{4 \sum_i \langle n_{\text{ryd}}(x_i) \rangle \cdot \langle n_{\text{ryd}}(x_i + \Delta x) \rangle}, \quad (2)$$

where $n_{\text{ryd}}(x_i)$ ($= 0$ or 1) is the Rydberg atom detected at the pixel position x_i in a single-shot image and $\langle \cdot \rangle$ is the ensemble average over single-shot images. Note that a factor of $5/4$ is included in Eq. (2) as there are only $N = 5$ Rydberg excitations and this factor of $\frac{N}{N-1}$ ensures that the correlation function is equal to 1 in the uncorrelated case. The pair correlation function $g^{(2)}(\Delta x)$ plotted in Fig. 4(c) clearly shows anti-bunching ($g^{(2)} < 1$) at small Δx , which is consistent with theory and due to the excitation blockade. Some bunching ($g^{(2)} > 1$) at large Δx implies positive correlation of exciting Rydberg superatoms. To further reveal the configuration of Rydberg superatoms in the 1D chain, we perform fast Fourier transform (FFT) on the spatial distribution of

the absorption spots due to Rydberg superatoms. The resulting FFT spectrum is shown in Fig. 4(d). A pronounced spectral peak at $1/\Delta x = 1/27.6 \mu\text{m}^{-1}$ indicates the most probable separation between two adjacent Rydberg superatoms. Moreover, the FFT of a simulated distribution with 5 regularly spaced peaks, as shown in Fig. 4(d), agrees well with the FFT of the experimental distribution. This FFT analysis demonstrates that Rydberg superatoms are excited in an ordered configuration with a nearly regular spacing of $\Delta x = 27.6 \mu\text{m}$, which is about $2R_{b-EX}^{r_0}$.

Additionally, in the inset of Fig. 4(d), we plot a similar FFT spectrum from experimental data of 4 and 6 Rydberg superatoms being detected per image. The position of the side lobe at $1/\Delta x = 1/27.6 \mu\text{m}^{-1}$ coincides with that of the spectrum from 5 regularly spaced Rydberg superatoms [34]. This suggests that Rydberg superatoms excited in such a cold-dense cloud tend to arrange in a quasi-crystallization pattern, which is generally compatible with theoretical predictions [33, 35]. Our imaging technique offers an alternative way to investigate highly-correlated Rydberg excitations [21].

IV. CONCLUSION

In conclusion, we have achieved single-shot imaging of individual Rydberg “superatoms” in an atomic ensemble by utilizing interaction enhanced absorption imaging in combination with homodyne detection. To reach the required signal-to-noise ratio for the detection of highly-lying $n'S$ Rydberg state excitations, electromagnetically induced transparency to low nF state in the vicinity of a strong Forster resonance was chosen. The technique can be used to detect a wide range of $n'S$ states and may be further improved by choosing lower-lying $n\ell$ states with larger ℓ . We have been able to image linear chains of up to five Rydberg excitations with an imaging fidelity of 93%. Long-range ordering was observed, suggesting onset of quasi-crystallization predicted in such systems. Further studies of time dynamics will be necessary for confirming this result. Our imaging technique could be applied for fast quantum state measurement of atomic qubits or superatom qubits.

V. ACKNOWLEDGEMENT

The authors thank Klaus Mølmer for useful discussions and acknowledge the support by the National Research Foundation, Prime Ministers Office, Singapore and the Ministry of Education, Singapore under the Research Centres of Excellence programme. Thibault Vogt received supports from National Natural Science Foundation of China under Grant No. 12174460.

Appendix A: Inter-state interaction potentials

We use the open-source *pairinteraction* software [36] to calculate the interaction potential due to the coupling of pair states near the $|rr'_0\rangle$ state, and the results are given in Fig. 5.

The non-interacting basis used for this calculation is constructed using all the pair states $|n_1, l_1, j_1, m_{j_1}; n_2, l_2, j_2, m_{j_2}\rangle$ energetically near $|rr'_0\rangle$, where $\Delta_{n_1} = |n_1 - 27| \leq 2$ & $\Delta_{l_1} = |l_1 - 3| \leq 2$, $\Delta_{n_2} = |n_2 - 96| \leq 2$ & $\Delta_{l_2} = |l_2 - 0| \leq 2$, and j_1 & m_{j_1} and j_2 & m_{j_2} take all valid values. This selection of the states results in a diagonalization space including over 2680 base vectors. These pair states are coupled together via electrical multiple interactions, the leading term of which is the dipole-dipole interaction. In Fig. 5(a), the potential curves close in energy to the $|rr'_0\rangle$ state are plotted versus the interatomic distance R for the case of $\theta = 90^\circ$. At large R , these energy levels asymptotically approach their unperturbed levels. At small R , interactions mix these states, and the energy level adiabatically evolved from the $|rr'_0\rangle$ state at $R \rightarrow \infty$ gets pushed upwards. Note that plotted in Fig. 1(b) is a simplified potential plot showing only the two most strongly dipole-coupled pair states for $R > 5 \mu\text{m}$.

Similar to that shown in Fig. 5(a), we calculate the set of potential curves for $\theta \neq 90^\circ$, and for each θ fit a van der Waals function $V^{rr'_0}(R) = -C_6^{rr'_0}/R^6$ to the upmost potential curve that asymptotically converges towards the $|rr'_0\rangle$ state at $R \rightarrow \infty$ (refer to Fig. 1(b)). The plot of the $C_6^{rr'_0}$ coefficients against θ is given in Fig. 5(b). It can be seen that the $C_6^{rr'_0}$ has the largest amplitude at $\theta = 90^\circ$ and the smallest one at $\theta = 0^\circ$.

Appendix B: Experimental setup and parameters

1. Preparation of the ground-state atomic cloud

We prepare a highly elongated, cylindrical cloud of atoms in the ground state $|g\rangle = |5S_{1/2}, F = 2, m_F = 2\rangle$ with a temperature of $25 \mu\text{K}$, which has been released from an optical dipole trap for a time of flight of $10 \mu\text{s}$ [27]. The cloud radially follows a Gaussian density distribution with a standard deviation of $\sigma_r = 6 \mu\text{m}$, axially extends a couple millimeters along the x direction, and has a peak density of $n_0 = 3.9 \times 10^{11} \text{ cm}^{-3}$ that corresponds to a mean interatomic distance of $\sim 0.85 \mu\text{m}$.

2. Excitation of Rydberg “superatoms”

The excitation energy level scheme is given at the left of Fig. 1(d). Rydberg excitations are induced with two lasers of wavelengths 780 nm and 479 nm , on resonance with the $|g\rangle \rightarrow |e\rangle = |5P_{3/2}, F = 3, m_F = 3\rangle$ and $|e\rangle \rightarrow |r'_0\rangle = |96S_{1/2}, m_J = 1/2\rangle$ (or $|e\rangle \rightarrow |r'_1\rangle = |85S_{1/2}, m_J =$

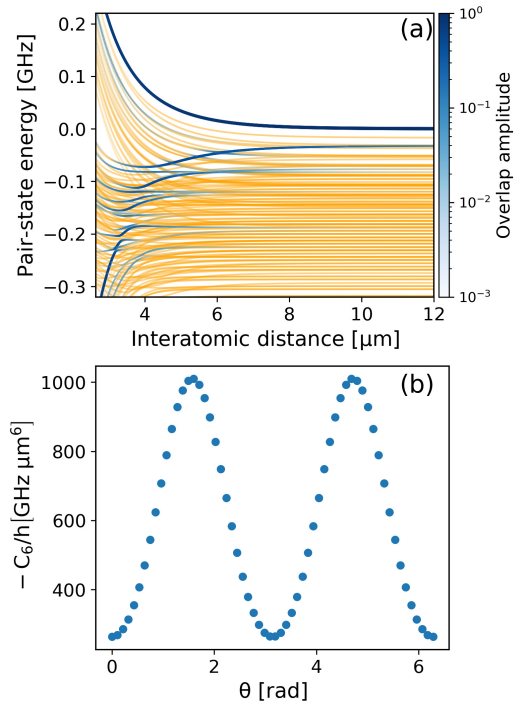


FIG. 5. (a) Calculated interaction potential curves for the pair state $|rr'_0\rangle$ at $\theta = 90^\circ$, where θ is the angle between the quantization axis and the internuclear axis of the pair. The color bar indicates the projection coefficient of a potential curve’s corresponding eigenstate onto the unperturbed pair state $|rr'_0\rangle$. (b) The amplitude of $C_6^{rr'_0}$ coefficient plotted versus θ .

$1/2\rangle$) transitions, respectively. While both lasers are pulsed on for a duration of $0.5 \mu\text{s}$, the 479-nm pulse is switched on and off first, leading the 780-nm pulse by 30 ns . The configuration of the excitation beams is given in Fig. 6.

Due to the interaction $V^{r'_0r'_0}(R) = -C_6^{r'_0r'_0}/R^6$ between two atoms in the $|r'_0\rangle$ state, there exists an excitation blockade sphere of radius $R_{b-EX}^{r'_0} = [2|C_6^{r'_0r'_0}|/\gamma_{EIT-EX}^{r'_0}]^{1/6}$, within which only one Rydberg excitation is allowed. Here $\gamma_{EIT-EX}^{r'_0} = \frac{(\Omega_{c-EX}^{r'_0})^2}{\Gamma}$, where $\Gamma = 2\pi \times 6.07 \text{ MHz}$ is the spontaneous decay rate of the intermediate state $|e\rangle$. About the same excitation blockade also arises when exciting the $|r'_1\rangle$ state.

TABLE I. Spatial parameters of the two excitation laser beams

Parameters	780 nm	479 nm
Propagation direction	$-\hat{y}$	\hat{x}
Polarization	\hat{x}	\hat{y}
$1/e^2$ radius	3.5 mm (before the slits)	31 μm

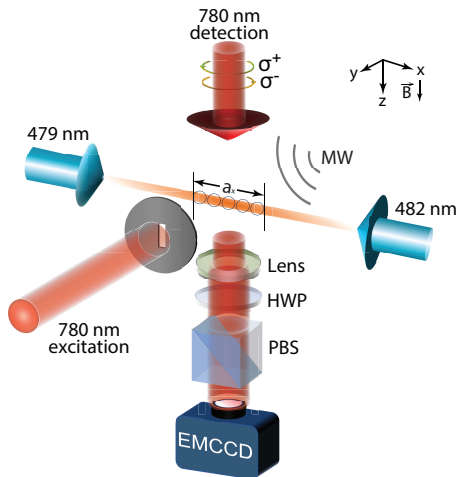


FIG. 6. Experimental setup. The configurations of the atomic ensemble, the laser beams and the homodyne imaging optics are the same as those in Ref. [27].

TABLE II. Rabi frequencies of the excitation laser beams and excitation blockade radii

Excited States	$\Omega_{P-EX}/2\pi$	$\Omega_{C-EX}/2\pi$	R_{b-EX}'
$ r_1'\rangle$	1.2 MHz	3.4 MHz	$14.4 \mu\text{m}$
$ r_0'\rangle$ (spectroscopy)	2.3 MHz	6.5 MHz	$14.7 \mu\text{m}$
$ r_0'\rangle$ (imaging)	2.3 MHz	6.5 MHz	$14.7 \mu\text{m}$

Tables I and II list the parameters of two excitation beams as well as the resulting excitation Rabi frequencies. In all the measurements of this paper, the excitation Rabi frequencies are set to give an excitation blockade radius $R_{b-EX}' = 14.5 \pm 0.2 \mu\text{m}$. In the high density atomic cloud of our experiment, there is, with nearly unity probability, one (and only one) Rydberg excitation within a blockade sphere of radius R_{b-EX}' , which is commonly termed as a Rydberg “superatom”. With the thin atomic cloud in our experiment, only one Rydberg superatom is allowed radially along the y and z directions, and Rydberg superatoms are closely packed to form an ordered array along the axial direction x [27, 32, 33, 37, 38]. The length of the atomic cloud segment exposed to the excitation laser can be adjusted, and so is the number of Rydberg superatoms. For the spectroscopic measurements, this length is set to $a_x = 350 \mu\text{m}$ to increase the number of Rydberg superatoms, which results in a better signal-to-noise ratio and speeds up the measurement process. This is especially necessary, since we don’t use homodyne detection here. Meanwhile, in the case of imaging individual Rydberg superatoms, the length is set to $a_x = 17 \mu\text{m}$ and $a_x = 126 \mu\text{m}$ to accommodate one Rydberg superatom and five Rydberg superatoms, respectively.

3. Parameters of the imaging fields

About $0.2 \mu\text{s}$ after the laser excitation, the detection pulses are turned on for $3 \mu\text{s}$. The detection level scheme relies on multi-photon Rydberg EIT as shown on the right of Fig. 1(d) with an effective two-photon coupling field driving the $|e\rangle \rightarrow |r\rangle = |27F_{7/2}, m_F = 7/2\rangle$ transition. For homodyne detection, the intensity ratio is experimentally optimized to be $r_{R-P_0} = 18$. Note that the recorded EIT images of the elongated atomic cloud have a 1-mm-wide field of view along the x direction, much larger than a_x .

Given in Table III is a list of all the relevant parameters in regard to the probe beam and the fields D and M that form the effective coupling field of Rabi frequency $\Omega_{C,\text{eff}} = 2\pi \times 5.9 \text{ MHz}$, in reference to the experimental configuration shown in Fig. 6.

TABLE III. Experimental parameters related to the detection fields

Parameters	Value / Unit
of the 780 nm probe beam	
Propagation direction	$+\hat{z}$
Polarization	$\hat{\sigma}^+$
$1/e^2$ radius	3.4 mm
Rabi frequency Ω_P	$2\pi \times 0.9 \text{ MHz}$
of the 482 nm beam (D field)	
Propagation direction	$-\hat{x}$
Polarization	\hat{y}
$1/e^2$ radius	$46.5 \mu\text{m}$
Frequency detuning Δ_D	$2\pi \times 24 \text{ MHz}$
Rabi frequency (σ^+ component) Ω_D	$2\pi \times 20.8 \text{ MHz}$
of the 112 GHz microwave (M field)	
Propagation direction	in the $\hat{x} - \hat{y}$ plane
Polarization	in the $\hat{x} - \hat{y}$ plane
Frequency detuning Δ_M	$-2\pi \times 26.8 \text{ MHz}$
Rabi frequency (σ^+ component) Ω_{M1}	$2\pi \times 27.4 \text{ MHz}$

Appendix C: Size of absorption spots

Besides the amplitude, we also compare the sizes of the images of Rydberg superatoms with those of the noise spots. We fit a 2D Gaussian distribution profile to the absorption spots in $\mathcal{T}(x, y)$ and extract their standard deviations σ_x and σ_y [27]. As shown in Fig. 7, the size distribution of the superatoms is quite different from that of the noises spots. The former extends over a large range and peaks around $\sigma_x = 2.5 \text{ pixels} = 6.2 \mu\text{m}$ and $\sigma_y = 2.1 \text{ pixels} = 5.2 \mu\text{m}$, while the latter is more localized and peaks around $\sigma_x = \sigma_y = 1.3 \text{ pixels} = 3.2 \mu\text{m}$. It can be seen that the two distributions are very distinct from each other. This means that in addition to the spots

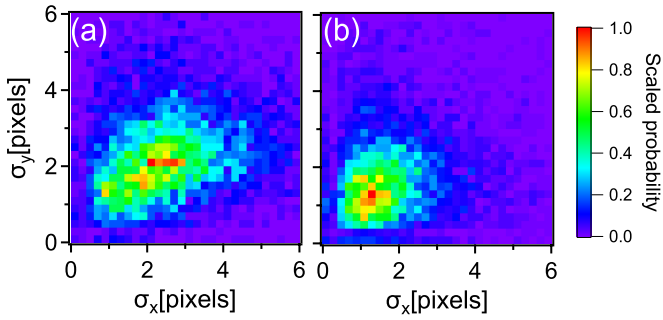


FIG. 7. Distribution of sizes σ_x & σ_y extracted from (a) images of Rydberg superatoms ($A_{peaks} > A_{thld}$) and (b) noise spots. The color bar indicates the normalized probability, where the value “1.0” corresponds to the distribution maxima in (a) and (b).

amplitudes, their sizes can also be used to differentiate the images of Rydberg superatoms from the noise speckles. Moreover, the sizes of spots are compatible

with the calculated interstate Rydberg blockade radius $R_{b-r'_0} = [2|C_6^{rr'_0}|/(\hbar\gamma_{EIT})]^{1/6} = 8.7 \mu\text{m}$.

Appendix D: Theoretical Model

The excitation of atoms in the deep blockade regime leads to the formation of highly ordered chains of Rydberg atoms. As shown experimentally, in a majority of cases the chains contain five Rydberg atoms. Based on this finding, the model of Fig. 4 makes the simplified assumption that five Rydberg superatoms are created exactly, the slit area of the atomic cloud that undergoes the excitation being divided into five regions of equal length, each containing exactly one Rydberg atom. The positions of the five atoms are obtained by direct sampling. For this, the position of each atom in a given subdivision is sampled randomly, according to a uniform distribution along the axial direction, and we reset the sample of the five atoms if the blockade condition is not fulfilled.

-
- [1] O. Firstenberg, C. S. Adams, and S. Hofferberth, Non-linear quantum optics mediated by rydberg interactions, *J. Phys. B* **49**, 152003 (2016).
- [2] M. Saffman, T. G. Walker, and K. Molmer, Quantum information with rydberg atoms, *Rev. Mod. Phys.* **82**, 2313 (2010).
- [3] A. Browaeys and T. Lahaye, Many-body physics with individually controlled rydberg atoms, *Nat. Phys.* **16**, 132 (2020).
- [4] T. F. Gallagher, *Rydberg Atoms* (Cambridge University Press, Cambridge, 1994).
- [5] M. D. Lukin, M. Fleischhauer, R. Cote, L. M. Duan, D. Jaksch, J. I. Cirac, and P. Zoller, Dipole blockade and quantum information processing in mesoscopic atomic ensembles, *Phys. Rev. Lett.* **87**, 037901 (2001).
- [6] T. Vogt, M. Viteau, J. Zhao, A. Chotia, D. Comparat, and P. Pillet, Dipole blockade at förster resonances in high resolution laser excitation of rydberg states of cesium atoms, *Phys. Rev. Lett.* **97**, 083003 (2006).
- [7] A. Gaëtan, Y. Miroshnychenko, T. W. an A. Chotia, M. Viteau, D. Comparat, P. Pillet, A. Browaeys, and P. Grangier, Observation of collective excitation of two individual atoms in the rydberg blockade regime, *Nat. Phys.* **5**, 115 (2009).
- [8] E. Urban, T. A. Johnson, T. Henage, L. Isenhower, D. D. Yavuz, T. G. Walker, and M. Saffman, Obsevation of rydberg blockade between two atoms, *Nat. Phys.* **5**, 110 (2009).
- [9] Y. O. Dudin and A. Kuzmich, Strongly interacting rydberg excitations of a cold atomic gas, *Science* **336**, 887 (2012).
- [10] T. Peyronel, O. Firstenberg, Q.-Y. Liang, S. Hofferberth, A. V. Gorshkov, T. Pohl, M. D. Lukin, and V. Vuletić, Quantum nonlinear optics with single photons enabled by strongly interacting atoms, *Nature* **488**, 57 (2012).
- [11] S. Baur, D. Tiarks, G. Rempe, and S. Dürr, Single-photon switch based on rydberg blockade, *Phys. Rev. Lett.* **112**, 073901 (2014).
- [12] D. Tiarks, S. Schmidt-Eberle, T. Stolz, G. Rempe, and S. Dürr, A photon–photon quantum gate based on rydberg interactions, *Nat. Phys.* **15**, 124 (2019).
- [13] H. Busche, P. Huillery, S. W. Ball, T. Ilieva, M. P. A. Jones, and C. S. Adams, Contactless nonlinear optics mediated by long-range rydberg interactions, *Nat. Phys.* **13**, 655 (2017).
- [14] S. Ebadi, T. T. Wang, H. Levine, A. Keesling, G. Semeghini, A. Omran, D. Bluvstein, R. Samajdar, H. Pichler, W. W. Ho, S. Choi, S. Sachdev, M. Greiner, V. Vuletić, and M. D. Lukin, Quantum phases of matter on a 256-atom programmable quantum simulator, *Nature* **595**, 227 (2021).
- [15] P. Scholl, M. Schuler, H. J. Williams, A. A. Eberharter, D. Barredo, K.-N. Schymik, V. Lienhard, L.-P. Henry, T. C. Lang, T. Lahaye, A. M. Läuchli, and A. Browaeys, Quantum simulation of 2d antiferromagnets with hundreds of rydberg atoms, *Nature* **595**, 233 (2021).
- [16] M. Kim, K. Kim, J. Hwang, E.-G. Moon, and J. Ahn, Rydberg quantum wires for maximum independent set problems, *Nat. Phys.* **18**, 755 (2022).
- [17] D. Bluvstein, S. J. Evered, A. A. Geim, S. H. Li, H. Zhou, T. Manovitz, S. Ebadi, M. Cain, M. Kalinowski, D. Hangleiter, J. P. B. Ataiades, N. Maskara, I. Cong, X. Gao, P. S. Rodriguez, T. Karolyshyn, G. Semeghini, M. J. Gullans, M. Greiner, V. Vuletić, and M. D. Lukin, Logical quantum processor based on reconfigurable atom arrays, *Nature* (2023).
- [18] A. Schwarzkopf, R. E. Sapiro, and G. Raithel, Imaging spatial correlations of rydberg excitations in cold atom clouds, *Phys. Rev. Lett.* **107**, 103001 (2011).
- [19] M. Stecker, H. Schefzyk, J. Fortágh, and A. Günther, A high resolution ion microscope for cold atoms, *New*

- Journal of Physics **19**, 043020 (2017).
- [20] C. Veit, N. Zuber, O. Herrera-Sancho, V. Anasuri, T. Schmid, F. Meinert, R. Löw, and T. Pfau, Pulsed ion microscope to probe quantum gases, *Physical Review X* **11**, 011036 (2021).
- [21] P. Schauß, M. Cheneau, M. Endres, T. Fukuhara, S. Hild, A. Omran, T. Pohl, C. Gross, S. Kuhr, and I. Bloch, Observation of spatially ordered structures in a two-dimensional rydberg gas, *Nature* **491**, 87 (2012).
- [22] H. Labuhn, D. Barredo, S. Ravets, S. de Léséleuc, T. Macrì, T. Lahaye, and A. Browaeys, Tunable two-dimensional arrays of single rydberg atoms for realizing quantum ising models, *Nature* (2016).
- [23] A. K. Mohapatra, T. R. Jackson, and C. S. Adams, Coherent optical detection of highly excited rydberg states using electromagnetically induced transparency, *Phys. Rev. Lett.* **98**, 113003 (2007).
- [24] G. Günter, H. Schempp, M. Robert-de Saint-Vincent, V. Gavryusev, S. Helmrich, C. S. Hofmann, S. Whitlock, and M. Weidemüller, Observing the dynamics of dipole-mediated energy transport by interaction-enhanced imaging, *Science* **342**, 954 (2013).
- [25] W. Xu, A. V. Venkatramani, S. H. Cantú, T. Šumarac, V. Klüsener, M. D. Lukin, and V. Vuletić, Fast preparation and detection of a rydberg qubit using atomic ensembles, *Phys. Rev. Lett.* **127**, 050501 (2021).
- [26] K. Srakaew, P. Weckesser, S. Simon Hollerith, D. Wei, D. Adler, I. Bloch, and Zeiher, A subwavelength atomic array switched by a single rydberg atom, *Nature Physics* **19** (2023).
- [27] J. Du, T. Vogt, and W. Li, Fast single-shot imaging of individual ions via homodyne detection of rydberg-blockade-induced absorption, *Phys. Rev. Lett.* **130**, 143004 (2023).
- [28] N. Šibalić, J. D. Pritchard, C. S. Adams, and K. J. Weatherill, Arc: An open-source library for calculating properties of alkali rydberg atoms, *Computer Physics Communications* **220**, 319 (2017).
- [29] J. D. Pritchard, D. Maxwell, A. Gauguet, K. J. Weatherill, M. P. A. Jones, and C. S. Adams, Cooperative atom-light interaction in a blockaded rydberg ensemble, *Phys. Rev. Lett.* **105**, 193603 (2010).
- [30] J. Han, T. Vogt, and W. Li, Spectral shift and dephasing of electromagnetically induced transparency in an interacting rydberg gas, *Phys. Rev. A* **94**, 043806 (2016).
- [31] A. Bergschneider, V. M. Klinkhamer, J. H. Becher, R. Klemt, G. Zürn, P. M. Preiss, and S. Jochim, Spin-resolved single-atom imaging of ^6Li in free space, *Phys. Rev. A* **97**, 063613 (2018).
- [32] D. Petrosyan and K. Mølmer, Stimulated adiabatic passage in a dissipative ensemble of atoms with strong rydberg-state interactions, *Phys. Rev. A* **87**, 033416 (2013).
- [33] D. Petrosyan, M. Hönig, and M. Fleischhauer, Spatial correlations of rydberg excitations in optically driven atomic ensembles, *Phys. Rev. A* **87**, 053414 (2013).
- [34] Images detected with 4, 5, and 6 Rydberg superatoms account for more than 80% of all experimental data.
- [35] M. Hönig, D. Muth, D. Petrosyan, and M. Fleischhauer, Steady-state crystallization of rydberg excitations in an optically driven lattice gas, *Phys. Rev. A* **87**, 023401 (2013).
- [36] S. Weber, C. Tresp, H. Menke, A. Urvoy, O. Firstenberg, H. P. Büchler, and S. Hofferberth, Calculation of rydberg interaction potentials, *Journal of Physics B: Atomic, Molecular and Optical Physics* **50**, 133001 (2017).
- [37] C. Ates and I. Lesanovsky, Entropic enhancement of spatial correlations in a laser-driven rydberg gas, *Physical Review A* **86**, 013408 (2012).
- [38] T. V. Vogt, J. Han, A. Thiery, and W. Li, Lévy statistics of interacting rydberg gases, *Physical Review A* **95**, 053418 (2017).